



Cu-Ni alloy nanocrystals with heterogenous active sites for efficient urea synthesis

Yulong Zhou^a, Baopeng Yang^c, Zhencong Huang^a, Gen Chen^a, Jianguo Tang^a, Min Liu^c,
Xiaohe Liu^d, Renzhi Ma^e, Zongwei Mei^{b,*}, Ning Zhang^{a,*}

^a School of Materials Science and Engineering, Central South University, Changsha 410083, China

^b Yangtze Delta Region Institute (Huzhou) & School of Physics, University of Electronic Science and Technology of China, Huzhou 313001, China

^c School of Physics and Electronics, Central South University, Changsha 410083, China

^d School of Chemical Engineering, Zhengzhou University, Zhengzhou 450001, China

^e International Center for Materials Nanoarchitectonics (MANA), National Institute for Materials Science (NIMS), 1-1 Namiki, Tsukuba, Ibaraki 305-0044, Japan

ARTICLE INFO

Keywords:

C–N coupling
Urea synthesis
Bimetallic catalyst
Active site
Copper alloy

ABSTRACT

Electrocatalytic urea synthesis from CO₂ and NO₃[−] are environmental green and energy savable. Although Cu are effective for CO₂ and NO₃[−] reduction reactions, achieving high efficiency of urea production remains challenging. Herein, Cu-Ni nanocrystals are formed to provide heterogenous active sites for promoting hydrogenation and C–N coupling reactions in urea synthesis. The carbon supported Cu-Ni nanocrystals are characterized by extended X-ray absorption fine structure and X-ray photoelectron spectroscopy spectra. The Cu-Ni nanocrystals achieves the highest urea Faradaic efficiency of 25.1 % and urea yield of 22.01 μmol h^{−1} cm^{−1}, which is much higher than that of single Cu or Ni metal. The reaction mechanism is probed by in-situ Fourier transform infrared spectroscopy, revealing a C–N coupling reaction pathway between *CO and *NH₂. Theoretical calculations suggest that hydrogenation of *NO_x and coupling *CO with *NH₂ are more easily occurred over co-existed Cu and Ni sites rather than homogeneous Cu or Ni site.

1. Introduction

Urea is an indispensable fertilizer and broadly utilized chemical, which plays an important role in human development [1,2]. In conventional industry, urea is synthesized by the Haber-Bosch reaction to produce ammonia (NH₃) and then the coupling reactions of NH₃ with CO₂ [3], which requires continuous high-energy input under harsh conditions [4–6]. The electrocatalytic synthesis of urea is a promising alternative to conventional urea synthesis due to its mild conditions and low energy consumption [6–8]. Particularly, electrocatalytic C–N coupling of greenhouse gases CO₂ and industrial effluent nitrate (NO₃[−]) to produce urea not only contributes to the target of carbon neutrality but also maximizes the utilization of waste resources [9–11].

Generally, the formation of urea includes the electrochemical reductions of CO₂ and NO₃[−] (e.g. CO₂ to CO and NO₃[−] to *NO_x), hydrogenation process (e.g. *NO_x to *NH_x, or *CONO to *CONH_x), and the C–N process (e.g. *NO₂ with *CO, or *NH₂ with *CO) [12,13]. To achieve high yield of urea, all these reactions should be high efficiency [14–16]. Up to now, plenty of materials such as Pb, Sn, Ag, Cu based metal and

compounds are developed as electrocatalysts for urea synthesis [17,18]. Among them, the Cu has been recognized as a cheap and efficient transition metals for CO₂ and NO₃[−] reduction reactions, which is promising for urea synthesis [18]. For instance, Cu metal atoms are suitable for adsorbing CO₂ to produce CO and hydrocarbons [19,20]. The Cu materials are also active for adsorbing NO₃[−] and further hydrogenating to form NH₃ [21]. More interestingly, it has been reported that the Cu electrocatalysts can achieve the C–N coupling to produce urea in presence of NO₃[−] and CO₂ [22]. However, achieving high-performance electrocatalysts for urea synthesis remains challenging for Cu materials, in significant part because the Cu active sites of materials are not satisfying the processes of C–N coupling reactions processes such as the *NO₂ with *CO or *NH₂ with *CO as well as the hydrogenation reactions on *NO_x or *CONO intermediates [13,14,23]. Properly tailoring active sites of Cu based materials to satisfy required C–N coupling and hydrogenation reactions is highly desirable for urea synthesis.

Recently, constructing heterogenous active sites are realizing effective strategy to minimize the reaction barriers, modify electronic state, and activate particular reactions. For instance, Zhang et al. found that

* Corresponding authors.

E-mail addresses: meizw@csj.uestc.edu.cn (Z. Mei), nzhang@csu.edu.cn (N. Zhang).

<https://doi.org/10.1016/j.apcatb.2023.123577>

Received 16 September 2023; Received in revised form 9 November 2023; Accepted 27 November 2023

Available online 29 November 2023

0926-3373/© 2023 Elsevier B.V. All rights reserved.

Fe@C and Fe₃O₄ formed on CNT provided dual active sites for adsorption and activation of NO₃⁻ and CO₂, resulting in the lower energy barriers of formed *NH₂ and *CO intermediates as well as the C–N coupling reactions [24]. Wang et al. found that bonded Fe–Ni pairs are effective sites for the synergistic adsorption and activation of multiple reactants, which thermodynamically and kinetically enhance the critical C–N coupling [14]. Although these significant work has been achieved, constructing heterogeneous active sites in Cu metals to promote the C–N coupling and hydrogenation reactions for efficient urea synthesis are still seldom concerned.

Herein, proper Ni content is incorporated into Cu to form Cu–Ni alloy, which provides heterogeneous active sites to promote the hydrogenation of NO_x species and C–N coupling reaction for urea synthesis. In detail, a carbon supported Cu–Ni catalysts are synthesized by pyrolysis of Cu–Ni metal-organic frameworks (MOF). The X-ray absorption spectroscopy (XAS) and X-ray photoelectron spectroscopy (XPS) show that Cu and Ni are mainly metallic states. The performance of urea synthesis for Cu–Ni catalyst is higher than those of individual metal of Cu and Ni electrocatalysts, which achieves Faradaic efficiency of producing urea as high as 25.1 % at –0.5 V (vs RHE) and yield of 37.53 μmolh⁻¹cm⁻² at –0.8 V (vs RHE). Such a performance is much superior to mostly reported catalysts. The mechanism of urea formation is analyzed by in situ Fourier transform infrared spectroscopy (FTIR), revealing a possible C–N coupling reaction pathway between *NH₂ and *CO. The theoretical calculations suggest that hydrogenation of *NO_x and coupling of *CO and *NH₂ are more easily occurred over the heterogeneous Cu and Ni atoms rather than on homogeneous Cu and Ni atoms. The designed heterogeneous active sites in this work provide a facile and highly efficient strategy for urea synthesis from NO₃⁻ and CO₂.

2. Experimental section

2.1. Preparation of Cu_xNi_y BTC

Preparation of monometallic and bimetallic MOFs as precursors by hydrothermal synthesis route [25]. For the synthesis of Cu BTC, Cu(NO₃)₂·3H₂O (4 mmol, 0.966 g) and BTC (4.5 mmol, 0.946 g) were dissolved in 30 mL of mixed aqueous solution, where water: DMF: ethanol was 1:1:1, and the obtained solution was sonicated for half an hour to obtain a clear blue solution. The blue solution was then transferred to a 50 mL PTFE-lined stainless steel hydrothermal autoclave and kept at 120 °C for 12 h. The blue Cu BTC precursor obtained by centrifugation was further washed three times with water and ethanol alternately and dried in an oven at 60 °C for 8 h. Ni BTC was prepared from Ni(NO₃)₂·6H₂O and BTC by the same method as Cu BTC preparation. The co-existence of Cu and Ni BTC was synthesized using a similar hydrothermal route by adding proper amount of Cu(NO₃)₂·3H₂O and Ni(NO₃)₂·6H₂O, which named as Cu_xNi_y BTC (x + y = 10, the x and y stand for the mole ratio of added Cu(NO₃)₂·3H₂O and Ni(NO₃)₂·6H₂O during the synthesis). The ratio of Cu and Ni in final products may have deviations in compared with the set ratio of Cu and Ni nitrates during synthesis.

2.2. Preparation of Cu_xNi_y/C catalysts

The above obtained BTC precursors were pyrolyzed under Ar/5 % H₂ atmosphere to obtain the corresponding carbon-loaded mono- and bimetallic catalysts. The specific operation is to place the synthesized precursors inside the porcelain boat, and then transfer them to the tube furnace, where the reaction is carried out at 500 °C for 3 h with a heating rate of 5 °C min⁻¹, the powder obtained is the target catalyst, which named as Cu_xNi_y/C. The actually ratio of Cu and Ni in Cu_xNi_y/C may have deviations in compared with the set ratio of Cu and Ni nitrates during synthesis of precursor.

2.3. Electrochemical measurements

In this work, the performance of electrocatalytic NO₃⁻ and CO₂ synthesis of urea was carried out by using CHI 760E as an electrochemical workstation. Hg/HgO (1 M KOH-filled) was used as the reference electrode, and a 1 × 1 cm² platinum sheet was used for the counter electrode. The area of working electrode is fixed at 0.25 cm². The working electrode was a dry carbon fiber paper (CFP) modified with catalysts. The catalyst (5 mg) was dispersed in 1 mL of a 1:1 mixture of water and ethanol, and then 20 μL of Nafion (5 wt% aqueous solution) was added and sonicated for 30 min to form a homogeneous ink. The CFP was coated with 50 μL and the catalyst loading was 1 mg cm⁻². The obtained working electrodes were vacuum dried at 60 °C for further use. Before the electrochemical test, the cathode chamber of the H-type cell was pre-saturated with the corresponding gases (Ar > 99.999 %, CO₂ > 99.999 %). During the catalytic process, the gas flow rate was maintained at 30 mL min⁻¹. All the potentials were measured against a Hg/HgO (1 M KOH solution filling) reference electrode and converted to RHE as follows: E_{RHE} = E_{Hg/HgO} + 0.098 + 0.059 × pH. The pH is 6.8 or 8.3 for the measurement with CO₂ or without CO₂ saturation, respectively. The scan rate for linear sweep voltammetry (LSV) tests was 10 mV s⁻¹. The cyclic voltammetry curves in electrochemical double-layer capacitance (C_{dl}) determination were measured in a potential window where no Faradaic process occurred in an electrolyte of 0.1 M KHCO₃ and 0.1 M KNO₃ at different scanning rates of 20, 40, 60, 80, 100, 120, 140, 160 mV s⁻¹.

DFT computational details, materials, characterizations, urea quantification, NH₃ quantification, NO₂⁻ quantification, FE and the yield rate of NH₃ calculations, and the in situ FTIR measurements are shown in [Supporting Information](#).

3. Results and discussion

A carbon-loaded bimetallic catalyst (Cu_xNi_y/C) was obtained by high-temperature pyrolysis under Ar/H₂ atmosphere using Cu_xNi_y benzene-1, 3, 5-tricarboxylic acid (BTC) as the precursor (Fig. S1) [25]. The prepared materials with different mole ratio of Cu and Ni were named as Cu/C, Cu₉Ni/C, Cu₈Ni₂/C, Cu₅Ni₅/C, and Ni/C. As shown in Figs. S2–3, the SEM images of the MOF precursors show a regular octahedral morphology, which is gradually distorted with the increasing doping of Ni. Subsequently, the carbon-loaded Cu–Ni alloys were obtained after pyrolysis under Ar/H₂ atmosphere. As illustrated in Fig. 1a, the Cu and Ni correspond to PDF#70–7038 and PDF#65–2865, respectively. The XRD patterns show that Cu/C, Ni/C, and Cu_xNi_y/C are pure metallic phases with face-centered cubic structure. As expected, the Cu (111) plane diffraction peak shifts to higher angle owing to the contraction of its lattice spacing after Ni incorporation. The scanning electron microscope (SEM) image shows the same octahedral morphology as the MOF precursor (Fig. 1b and Fig. S4). The magnified SEM (Fig. 1c and Fig. S4) shows that the octahedral structure of the catalyst is consisted of stacked nanoparticles with size about 20–50 nm. The TEM image in Fig. 1d and Fig. S5 confirms that the aggregated nanoparticles are formed after pyrolysis. As illustrated in Fig. 1e, the high-resolution TEM (HR-TEM) image illustrates that Cu–Ni nanoparticle presents clear lattice fringes with a plane distance of 0.21 nm, which corresponds well to the (111) plane of cubic Cu (Fig. S6). The fast Fourier transform (FFT) pattern exhibits the cubic structure of Cu metal with (111) plane exposed in Cu₈Ni₂/C [12,26]. The transmission electron microscopy (TEM) and the corresponding EDX mapping images shows that Cu and Ni elements are well distributed in Cu_xNi_y/C (Fig. 1f, Fig. S7).

The element states of formed Cu₈Ni₂/C catalysts were further investigated by X-ray absorption spectroscopy (XAS). Fig. 2a presents the normalized Cu K-edge X-ray near-edge absorption structure (XANES) spectra of Cu₈Ni₂/C, Cu foil, CuO, and Cu₂O. The absorption edge of Cu in Cu₈Ni₂/C is negatively shifted by ~0.3 eV compared with that of Cu

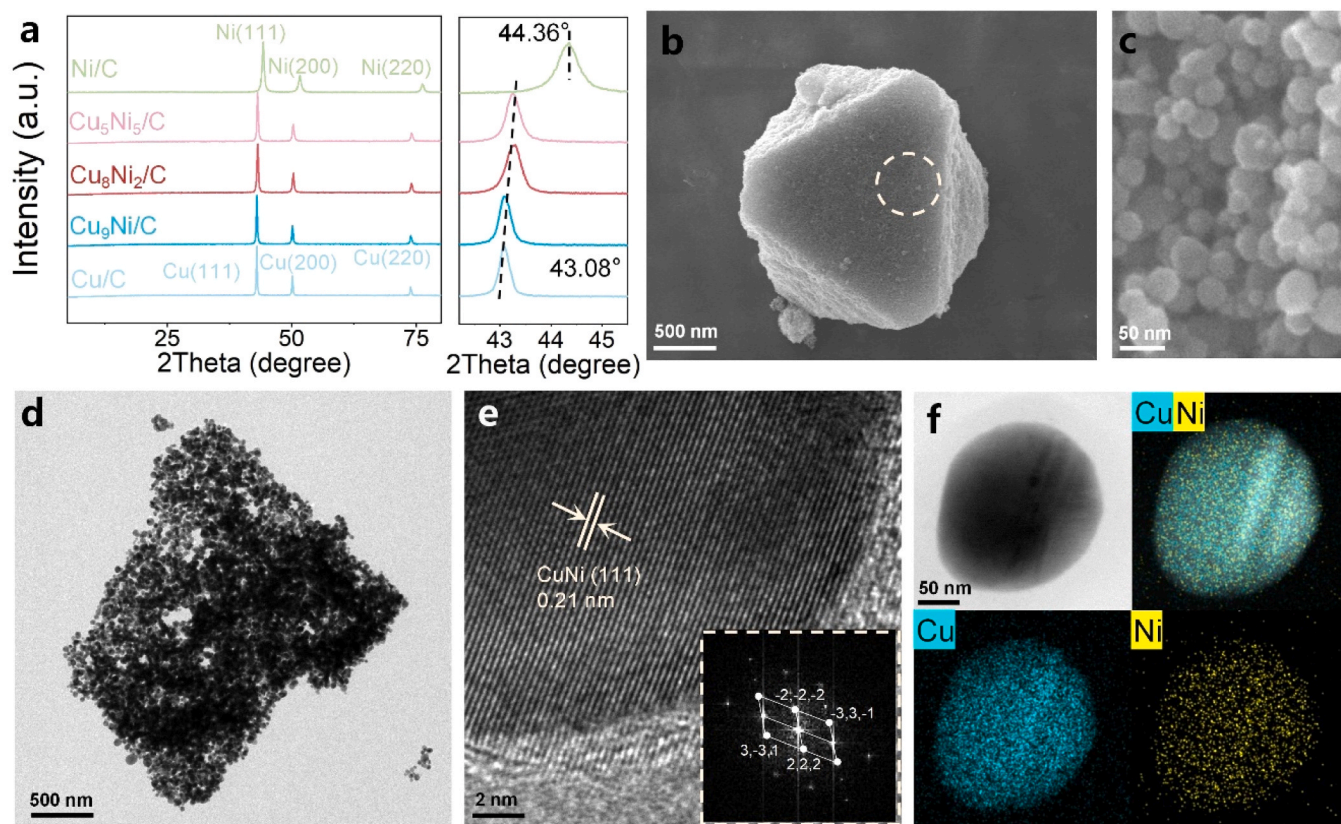


Fig. 1. Morphology and structure of catalysts. (a) XRD pattern of Cu/C, Cu₉Ni/C, Cu₈Ni₂/C, Cu₅Ni₅/C and Ni/C catalysts with enlarged (111) crystal plane. (b) SEM image, (c) local enlargement image, (d) TEM image, (e) High-resolution TEM image of Cu₈Ni₂/C. (f) TEM image and corresponding elemental mappings of Cu₈Ni₂/C, where Cu and Ni atoms are represented by blue and yellow pixels, respectively.

foil. However, the normalized K-edge XANES of Cu₈Ni₂/C shows that the corresponding absorption edge of Ni is positively shifted compared to the Ni foil (Fig. 2b). In addition, the first-order derivative of XANES shows that the valence states of Cu and Ni elements in Cu₈Ni₂/C are the same as those of Cu and Ni foils (0 valence state), which are lower than those of copper oxides (Cu₂O and CuO) and nickel oxide (NiO) as shown in Fig. 2c,d [27]. These results indicate that both Cu and Ni are metallic states and a redistribution of electrons from Ni to Cu in Cu₈Ni₂/C. Moreover, Fourier transform of expanded X-ray absorption fine structure (FT-EXAFS) characterizations show a bond length (2.24 Å) of Cu₈Ni₂/C between the Cu-Cu (2.27 Å) in Cu foil and Ni-Ni (2.18 Å) in Ni foil, further confirming the formation of CuNi solid solution (Fig. 2e). Additionally, the metallic bonds of the synthesized Cu-Ni alloys are quite different from the Cu-Cu bonds in copper oxides (Cu₂O and CuO) and Ni-Ni bonds in nickel oxide (NiO) [28,29]. Moreover, Wavelet transform (WT)-EXAFS was conducted to identify the metal-metal and metal-O bonds in Cu₈Ni₂/C and related references. The WT-FXAFS analysis clearly illustrates that Cu₈Ni₂/C is conformationally consistent with Cu or Ni foil and distinguished from the Cu and Ni oxides (Fig. 2f and S8). The above results further confirm the formation of Cu-Ni alloy in Cu₈Ni₂/C. The electronic structure of the Cu₈Ni₂/C catalyst was further evaluated by X-ray photoelectron spectroscopy (XPS). For energy calibration, the position of C1s photoelectron peak was applied (binding energy 284.8 eV, Fig. S9). Notably, the 2p peak of Ni⁰ moves toward higher binding energy with increasing Cu content, whereas the 2p peak of Cu⁰ moves toward lower binding energy (Fig. 2g and S10), implying that Cu and Ni in Cu₈Ni₂/C lead to electron redistribution because of the alloying effect [30–32]. The result is also consistent with XAS, where electrons aggregate from Ni to Cu.

The electrochemical measurements were carried out in the classical three-electrode system (Fig. S11), where the counter electrode was

1 × 1 cm² platinum sheet and reference electrode was Hg/HgO. The concentrations of urea, nitrite, and ammonium were calibrated by diacetyl monoxime [6,33], N-(1-naphthyl)-ethylenediamine dihydrochloride [34], and indophenol blue methods [35], respectively (Fig. S12). Notably, when using the diacetyl monoxime method to calibrate urea, high nitrite concentrations may influence urea calibration. It is necessary to ensure that the nitrite concentration is less than 100 μmolL⁻¹ in the measurement system for diacetyl monoxime method [36]. Meanwhile ¹H NMR chemical shift in the range of 5.1–5.2 and control tests without NO₃⁻/CO₂ was used to further confirm the urea production (Fig. S13) [12].

Linear sweep voltammetry (LSV) tests were performed to evaluate the electrochemical behaviours of Cu, Ni, and Cu-Ni bimetallic catalysts in CO₂-saturated electrolyte with 0.1 M KHCO₃ + 0.1 M KNO₃ at a scan rate of 10 mV s⁻¹. As shown in Fig. 3a, the current density is decreased in the order of Cu₅Ni₅/C, Cu₈Ni₂/C, Cu, Cu₉Ni/C, and Ni. Note that the current density shows in Fig. 3a is contributed by the various electrocatalytic reactions, such as urea synthesis, hydrogen evolution reaction (HER), CO₂ reduction reactions (CO₂RR), and NO₃⁻ reduction reactions (NO₃RR). As shown in Fig. 3b, the Tafel slopes are 162.12, 219.78, 276.87, 286.62, and 465.45 mV dec⁻¹ for Cu₈Ni₂/C, Cu₅Ni₅/C, Cu, Cu₉Ni/C, and Ni. The Tafel slope represents the total kinetic process of these reactions including HER, CO₂RR, and NO₃RR, and the side reactions play an important role in providing key intermediates in the urea synthesis process. Thus, the Tafel slope results indicate that the Cu-Ni alloys shows relatively higher overall electrocatalytic activity than the single Cu or Ni. Taking Cu₈Ni₂/C material as an example, then control experiments were carried out to check the effect of reactants on current density as shown in Fig. 3c. A relatively low current density is produced in Ar saturated electrolyte without NO₃⁻, which is mainly attributed to the HER and slightly lower than the CO₂RR performance (CO₂ without

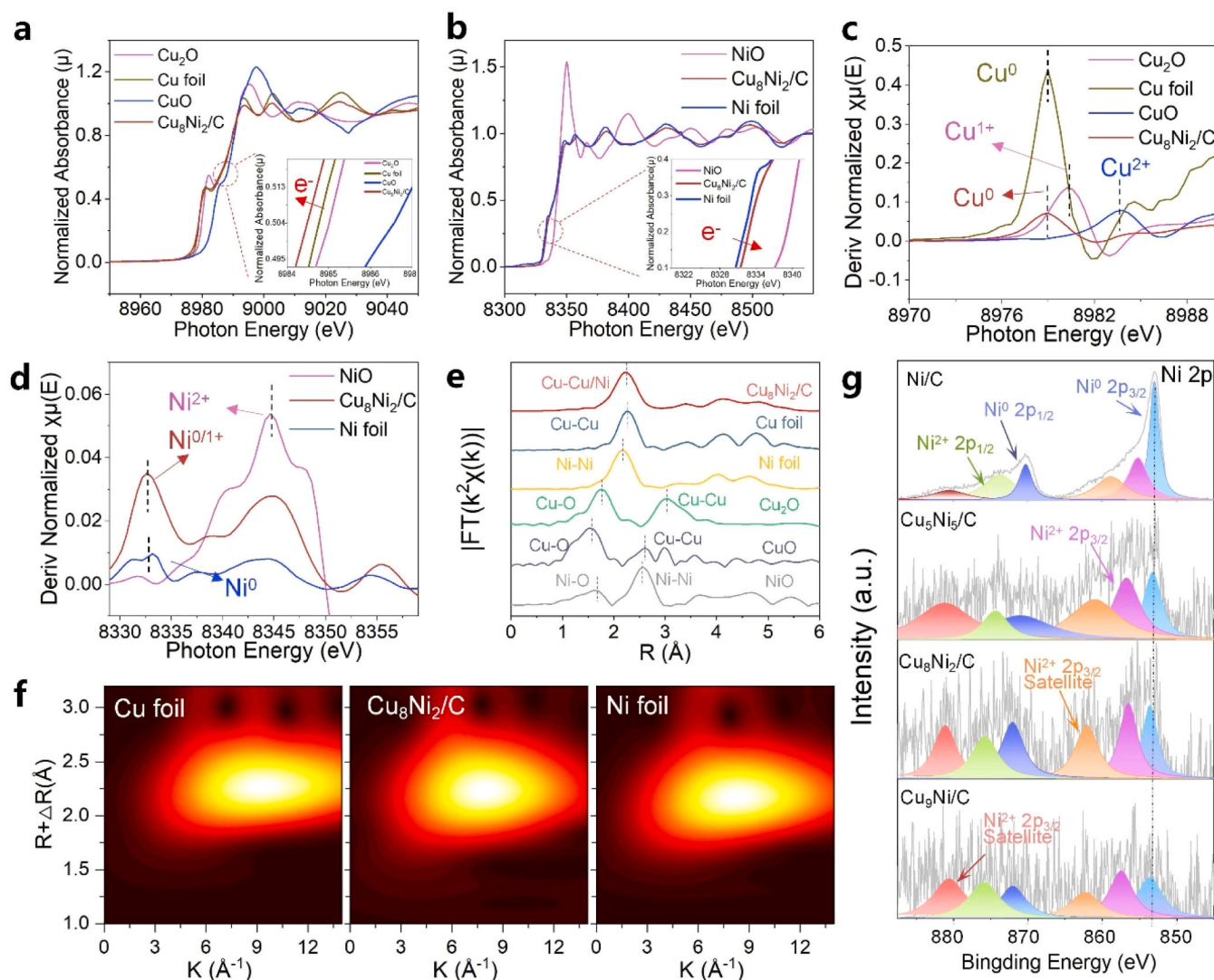


Fig. 2. Electron transfer and valence state of catalysts. (a) Normalized and (c) deriv-normalized intensity Cu K-edge X-ray absorption near-edge structure (XANES) spectra for Cu₂O, CuO, Cu foil and Cu₈Ni₂/C. (b) Normalized and (d) deriv-normalized intensity of Ni K-edge XANES spectra for NiO, Ni foil and Cu₈Ni₂/C. (e) Fourier transform extended X-ray absorption fine structure (FT-EXAFS) spectra of Cu₈Ni₂/C and other references. (f) Wavelet-transform plots for Cu foil, Cu₈Ni₂/C, and Ni foil. (g) XPS peaks spectra of Ni 2p of Cu/C, Cu₉Ni/C, Cu₈Ni₂/C, Cu₅Ni₅/C.

KNO₃). A partial enlargement of Fig. 3c is shown in Fig. S14. It is noting that the current density of HER improves with the increase of Ni component in Cu-Ni alloy (Fig. S15), which indicates that the doping Ni is favorable to the HER process from water splitting. There is no obviously current improvement when the solution is the saturated CO₂ without NO₃⁻. The reactions are mainly HER and CO₂RR in such a condition. In presence of NO₃⁻ and Ar, the current is improved greatly, which is mainly ascribed to the NO₃RR and HER. When both NO₃⁻ and CO₂ are co-existent, the current is decreased in compared with the existence of NO₃⁻ and Ar, which may be caused by the sluggish of urea formation.

The produced urea is examined over various potentials and materials. At potential from -0.4 to -0.8 V (vs RHE), there is a volcano distribution among Cu-Ni alloys and the highest activity is located at the Cu₈Ni₂/C. The Faradaic efficiency (FE) and yield rate reaches as high as 25.1 % with a urea yield rate of 22.01 μmol h⁻¹ cm⁻¹ at -0.5 V (vs RHE) on Cu₈Ni₂/C (Fig. 3d). Furthermore, the urea yield on Cu₈Ni₂/C catalyst increases with more negative potential, reaching 37.53 μmol h⁻¹ cm⁻¹ at -0.8 V (vs RHE) as shown in Fig. 3d. The FE(urea) and urea yield rate are relatively stable at -0.5 V (vs RHE) during the test of 10 cycles as shown in Fig. 3e. The corresponding I-t curves are shown in Fig. S16.

These results indicate that Cu₈Ni₂/C exhibits good electrocatalytic stability for urea synthesis from CO₂ and NO₃⁻. In comparison with other reported efficient catalysts (half of which are copper materials), Cu₈Ni₂/C has the superior urea yield rate of (37.53 μmol h⁻¹ cm⁻¹) at (-0.8 V) with FE in the middle range (Fig. 3f). The concrete measurement parameters and performance are shown in Supplementary Table S1.

As illustrated in Fig. S17, the Faraday efficiency for nitrite (FE(NO₂⁻)) on Cu/C at -0.4 V reaches 79.36 %, which implies that the Cu active site is weak for *NO₂ adsorption or difficult to continue the conversion of *NO₂, resulting in a high selectivity for nitrite on Cu/C catalyst.[11]. As the content of Ni increased in the Cu_xNi_y/C bimetallic catalyst, the selectivity for nitrite decreased. And the ratio of FE(NO₂⁻) to the sum of FE(NH₃) and FE(urea) decreased from 4.5 to 0.86 (Fig. S18). This observation suggests that Ni favors the adsorption of *NO₂ and the subsequent hydrogenation process for the conversion to *NH₂. In addition, the electrochemical impedance spectroscopy (EIS) was tested at -0.4 V (vs RHE), as shown in Fig. S19. The charge transfer resistance is decreases with the increase of Ni content in Cu-Ni materials, which will accelerate the electrocatalytic reactions. The double-layer capacitance (C_{dl}) was used to calculate the electrochemically active surface area (ECSA) of electrocatalysts. For urea synthesis, the Cu₈Ni₂/C sample

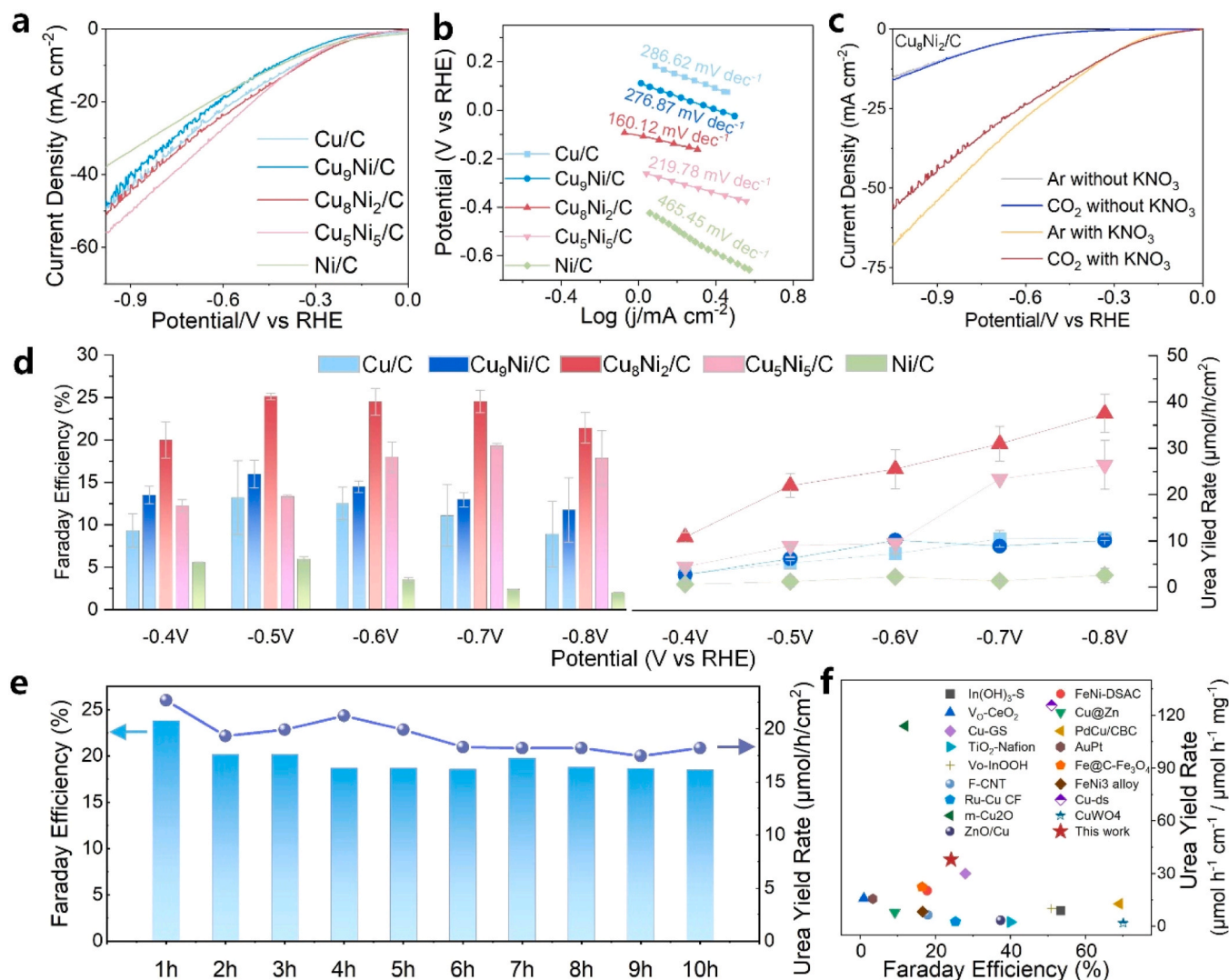


Fig. 3. Electrocatalytic performances of urea synthesis. (a) LSV curves over Cu/C, Cu₉Ni/C, Cu₈Ni₂/C, Cu₅Ni₅/C, and Ni/C catalysts (catalysts loading was 1 mg cm⁻²) measured in 0.1 M KHCO₃ + 0.1 M KNO₃ electrolyte at a scan rate of 10 mV s⁻¹ (b) Tafel slopes of Cu/C, Cu₉Ni/C, Cu₈Ni₂/C, Cu₅Ni₅/C, and Ni/C in the electrolyte of 0.1 M KHCO₃ + 0.1 M KNO₃. (c) LSV curves over Cu₈Ni₂/C (catalysts loading was 1 mg cm⁻²) in different variables (the solution concentrations were 0.1 M) at a scan rate of 10 mV s⁻¹. (d) Urea Faraday efficiencies and corresponding yield rate on Cu/C, Cu₉Ni/C, Cu₈Ni₂/C, Cu₅Ni₅/C, and Ni/C at various applied potentials (vs RHE) for 30 min of electrocatalysis. (e) FE(Urea) and yield rate on Cu₈Ni₂/C under the applied potential of -0.5 V (vs RHE) during 10 periods of 1 h electrocatalytic. (f) Comparison of the performance of Cu₈Ni₂/C catalyst with other extensively reported electrocatalysts for electrocatalytic nitrate and CO₂ synthesis of urea.

exhibits the highest C_{dl} (506.5 $\mu\text{F cm}^{-2}$). Generally, a larger C_{dl} represents higher catalytic area (ECA), which provide more abundant active sites for electrochemical reaction (Fig. S20).

Subsequently, the effect of nitrate concentration on the selectivity was further explored. The experiments were carried out with different NO_3^- concentration (100 mM, 20 mM and 4 mM) while keeping the KHCO_3 concentration at 100 mM. The experimental results showed that the current density and Faradaic efficiency of urea showed an increasing trend with increasing NO_3^- concentration (Fig. S21a, b). However, the highest selectivity for NH_3 production is found at the lowest NO_3^- concentrations (Fig. S21c). Probably, $^*\text{NH}_2$ intermediates were inhibited to achieve C–N coupling at its lower concentration, which then tended to be converted to NH_3 . It is worth noting that the concentration of nitrate also affects the NO_2^- selectivity, and there is an optimal NO_3^- concentration in the interval of 4–100 mM for the highest NO_2^- selectivity.

To explore the realistic surface states, in situ Raman spectroscopy was applied to analyze the surface of Cu–Ni catalyst during the reaction (Fig. S22). Raman spectra were tested at 0.2 V intervals from the open-

circuit potential, and the results showed that the catalyst surface state was stable under electrochemical action [37,38]. Furthermore, we employed ITO conductive glass as the substrate for catalyst loading, and the XRD pattern of the catalyst before and after electrochemical testing is presented in Fig. S23. These results indicate that there is no shift of peak positions and new peaks after the reaction, except the decreased intensity of Cu₈Ni₂ diffraction signal resulting from the possible drop of catalysts from ITO during the electrochemical test. A comparison of the morphology before and after the electrochemical reaction is shown in Fig. S24, where the catalyst consists of spherical particles stacked in a loose framework before the electrochemical reaction. After the electrochemical reaction, the particles were partially aggregated. In other words, the Cu₈Ni₂/C catalyst showed stable crystal phase with morphology reconstructure during the electrochemical reactions.

In situ FTIR measurements were carried out on Cu₈Ni₂/C, Cu/C, and Ni/C catalysts to investigate the evolution of intermediates during the C–N coupling process. The IR signal is collected every 0.1 V interval from the open circuit potential to -0.8 V (vs RHE) during the electrochemical

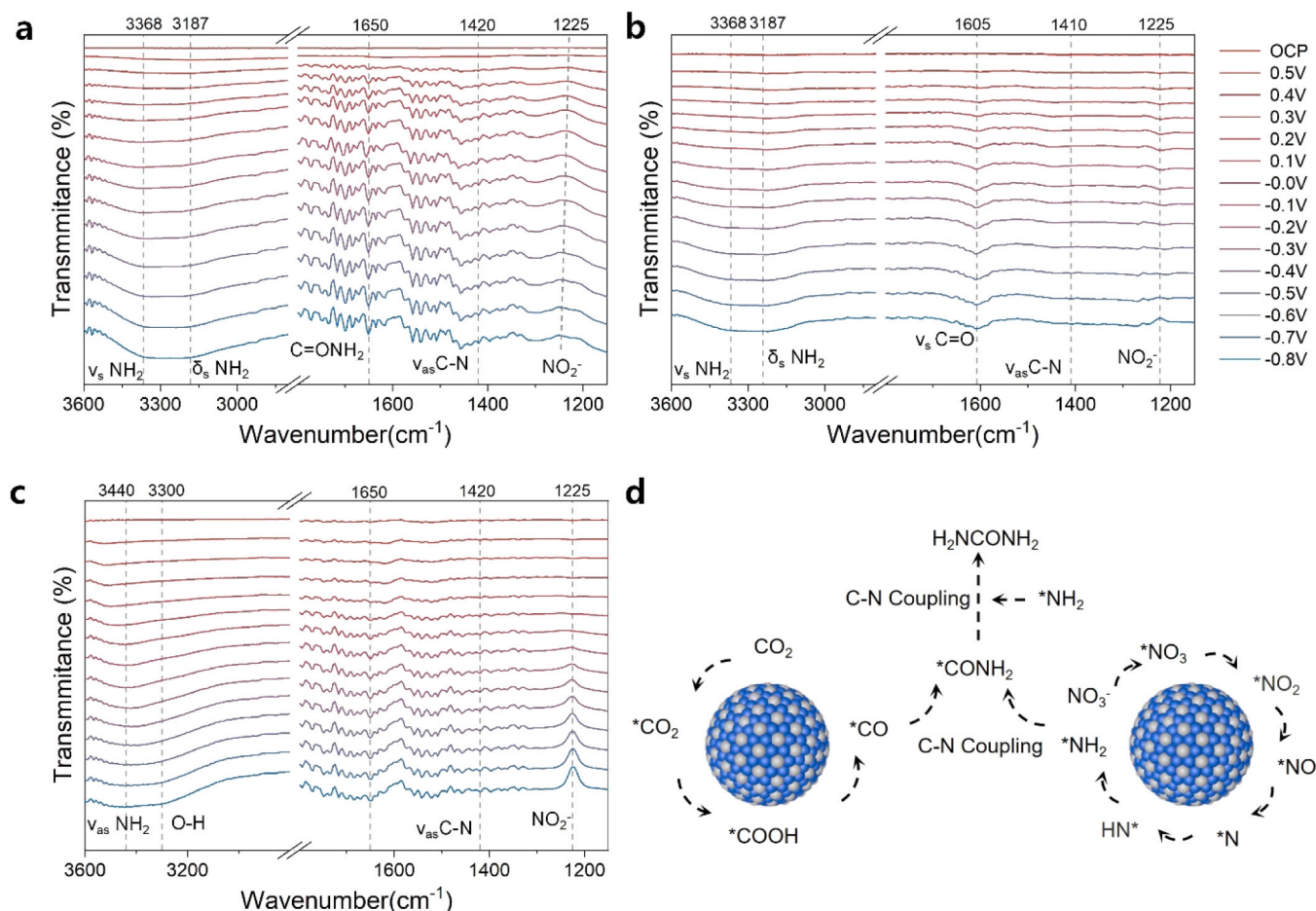


Fig. 4. In situ electrochemical spectroscopy measurements. Infrared signal in the range of 1000–3600 cm^{-1} (disconnected at 1800–2800 cm^{-1}) under various potentials for (a) $\text{Cu}_8\text{Ni}_2/\text{C}$, (b) Cu/C and (c) Ni/C during the electrocoupling of nitrate and CO_2 . (d) Proposed reaction pathway for urea formation on $\text{Cu}_8\text{Ni}_2/\text{C}$.

test. Fig. 4a–c show the in situ IR test results of $\text{Cu}_8\text{Ni}_2/\text{C}$, Cu/C , and Ni/C catalysts in CO_2 -saturated electrolyte with 0.1 M KNO_3 and 0.1 M KHCO_3 . The control experiment was also carried out by the in situ IR tests for $\text{Cu}_8\text{Ni}_2/\text{C}$ in 0.1 M KNO_3 + 0.1 M KHCO_3 electrolyte without CO_2 (Fig. S25). In the range of 1000–1300 cm^{-1} , all spectra showed distinct infrared bond around 1225 cm^{-1} ascribed to the anti-symmetric stretching vibration of N–O in nitrite during the reduction of NO_3^- to $^*\text{NO}_2$ (Fig. 4a–c and Fig. S25). This result indicates that $^*\text{NO}_2$ is an essential intermediate for the reduction of NO_3^- and urea synthesis [39]. In Fig. 4b, the IR spectra of Cu/C appears as a downward peak (formation of $^*\text{NO}_2$) from 0.4 V to -0.4 V and shift to an upwards peak (consumption of $^*\text{NO}_2$) as the potential decreases to lower than -0.7 V, indicating that the accelerated transition of $^*\text{NO}_2$ to $^*\text{NH}$ ($^*\text{NH}_2$) at the overpotential lower than -0.7 V. Notably, the upward peak (consumption of $^*\text{NO}_2$) starts at 0 V on the Ni/C (Fig. 4c) and becomes stronger with decreasing potential, which corresponds to the accelerated consumption of $^*\text{NO}_2$. However, the wave number belonging to $^*\text{NO}_2$ consumption gradually moves to larger ones (blue-shift) as increasing the negative potential from -0.6 V for the synthesis of urea on $\text{Cu}_8\text{Ni}_2/\text{C}$, which indicates the weaker absorption ability of $^*\text{NO}_2$ on the catalyst surface [40]. This is consistent with its decreased FE(urea) and increased FE(NH_3) at more negative potential (Fig. S17).

Based on the electrocatalytic performance, the $^*\text{NO}_2$ is consumed to produce the $^*\text{NH}$ and $^*\text{NH}_2$ intermediates for urea and NH_3 synthesis. According to consumption signal of $^*\text{NO}_2$, it can be concluded that Ni promotes the conversion of $^*\text{NO}_2$ to $^*\text{NH}$ ($^*\text{NH}_2$) at lower overpotential than Cu (Fig. 4a–c). Furthermore, in Fig. 4a, the infrared signals are observed around 3180 and 3350 cm^{-1} for $\text{Cu}_8\text{Ni}_2/\text{C}$ (with CO_2), which

are ascribed to the bending mode of NH_2 ($\delta_s \text{NH}_2$) and the NH_2 stretching mode ($\nu_s \text{NH}_2$), respectively [6,41]. Remarkably, these downward peaks were not observed in $\text{Cu}_8\text{Ni}_2/\text{C}$ (without CO_2 , Fig. S25), which can be judged that the peaks at 3180 and 3350 cm^{-1} are the N–H signals from urea molecule rather than the intermediates for urea or ammonia synthesis [1,14]. For Cu/C , the same $\nu_s \text{NH}_2$ and $\delta_s \text{NH}_2$ are correspondingly detected at 3368 and 3187 cm^{-1} , which show lower signal intensity and consequently less urea product than $\text{Cu}_8\text{Ni}_2/\text{C}$ (Fig. 4a, b and Fig. 3d). However, the infrared spectrum at 3440 cm^{-1} for Ni/C belongs to the NH_2 asymmetric stretching mode ($\nu_{as} \text{NH}_2$) acting as the intermediate for urea synthesis [6], which is not observed on Cu/C and $\text{Cu}_8\text{Ni}_2/\text{C}$ (Fig. 4a–c). It reveals that Ni is beneficial to the formation of $^*\text{NH}_2$ intermediate. Besides, the downward peak at 3300 cm^{-1} originates from the stretching vibration of the O–H of the associated state [42,43], which may be caused by the hydrolysis of Ni atoms to produce $^*\text{H}$ and O–H. The $^*\text{H}$ gets transferred and the associative state O–H accumulates on the catalyst surface. In sum, the Ni active sites in $\text{Cu}_8\text{Ni}_2/\text{C}$ promote the formation of $^*\text{NH}_2$ and accordingly enhance the electrocatalytic activity for urea synthesis.

Subsequently, the infrared band of Cu/C at 1605 cm^{-1} is assigned to C=O stretching vibration in $^*\text{CO}$ intermediate [44], which is not detected on $\text{Cu}_8\text{Ni}_2/\text{C}$ and Ni/C (Fig. 4a–c). It suggests that the moderate adsorption of $^*\text{CO}$ on Cu atoms. In addition, $\text{Cu}_8\text{Ni}_2/\text{C}$, Ni/C , and Cu/C show downward peaks indicating the formation of C–N with asymmetric stretching vibration at 1420 cm^{-1} , 1410 cm^{-1} , and 1420 cm^{-1} , respectively. It reveals that the C–N coupling is successfully achieved [6,45]. Note that the signal intensity of C–N on $\text{Cu}_8\text{Ni}_2/\text{C}$ is stronger than those on Cu/C and Ni/C , which may be resulted from the synergistic

effect of Cu and Ni for the correspondingly optimal formation of $^*\text{CO}$ and $^*\text{NH}_2$ intermediates.

At the end, the obvious infrared bond located at 1650 cm^{-1} on $\text{Cu}_8\text{Ni}_2/\text{C}$ is attributed to the $\text{C}=\text{O}$ stretching vibration of the amide I band ($^*\text{CONH}_2$) [46,47], which confirms the formation of $^*\text{CONH}_2$ intermediate (Fig. 4a). The $^*\text{CONH}_2$ intermediate may be a product of the first C–N coupling of $^*\text{CO}$ and $^*\text{NH}_2$. Based on the intermediates detected in the IR spectra, we summarize a reaction path for the synthesis of urea, as illustrated in Fig. 4d. In such a pathway, the CO_2 is firstly reduced to form $^*\text{CO}$ through $\text{CO}_2 \rightarrow ^*\text{CO}_2 \rightarrow ^*\text{COOH} \rightarrow ^*\text{CO}$, and NO_3^- is reduced to $^*\text{NH}_2$ through $\text{NO}_3^- \rightarrow ^*\text{NO}_3 \rightarrow ^*\text{NO}_2 \rightarrow ^*\text{NO} \rightarrow ^*\text{N} \rightarrow ^*\text{NH} \rightarrow ^*\text{NH}_2$. Then the $^*\text{CO}$ and $^*\text{NH}_2$ are directly coupled to form $^*\text{CONH}_2$. At last, the urea ($\text{CONH}_2)_2$ is synthesized by further $^*\text{NH}_2$ coupling on $^*\text{CONH}_2$ intermediate. We verify the feasibility of this reaction pathway, and analyze the reaction mechanism through subsequent DFT calculations.

Density functional theory (DFT) calculations were carried out to probe the reaction mechanism of C–N coupling for urea synthesis from NO_3^- and CO_2 . The Cu_{64} , Ni_{64} , and $\text{Cu}_{48}\text{Ni}_{16}$ slabs are built as models to study the properties of Cu, Ni, and Cu–Ni alloys, respectively. We

established calculation models based on the (111) surface of Cu, Ni, and Cu–Ni alloy (Fig. S26), which is a highly active face [48]. Firstly, the Table S2 shows the detailed adsorption models of the intermediates for the reduction of nitrate to $^*\text{NH}_2$, which present a process $\text{NO}_3^- \rightarrow ^*\text{NO}_3 \rightarrow ^*\text{NO}_2 \rightarrow ^*\text{NO} \rightarrow ^*\text{N} \rightarrow ^*\text{NH} \rightarrow ^*\text{NH}_2$. The key adsorption models are presented in Fig. 5a. In Cu and Ni metals, the $^*\text{NO}_x$ and $^*\text{NH}_2$ homogeneously bond with the Cu or Ni atoms. As for Cu–Ni alloy, the $^*\text{NO}_x$ and $^*\text{NH}_2$ prefer to heterogeneously bond with both Cu and Ni atoms in DFT optimization process. The Gibbs free energy for each step is presented in Fig. 5b. For Cu, the reduction of $^*\text{NO}_2$ to $^*\text{NO}$ is the rate-determining step (RDS) with a high Gibbs free energy change (ΔG) of 1.95 eV for the formation of $^*\text{NH}_2$. The high energy barrier for the conversion of $^*\text{NO}_2$ to $^*\text{NH}_2$ on Cu electrocatalyst, resulting in the desorption tendency for $^*\text{NO}_2$ from Cu surface to produce NO_2^- . Such a result is consistent with the results of the performance tests of the Cu catalyst ($\text{FE}(\text{NO}_2^-) = 79.36\%$) (Fig. S17). On the contrary, the ΔG are -0.32 eV and -0.12 eV on Ni and Cu–Ni alloy for the formation of $^*\text{NO}$ from $^*\text{NO}_2$, respectively. The result shows that Ni atoms are important in promoting the conversion of $^*\text{NO}_2$ to $^*\text{NH}_2$, which has been confirmed by insitu IR analysis as Fig. 4c presented. The formation of $^*\text{H}$ is shown in Fig. 5e, it

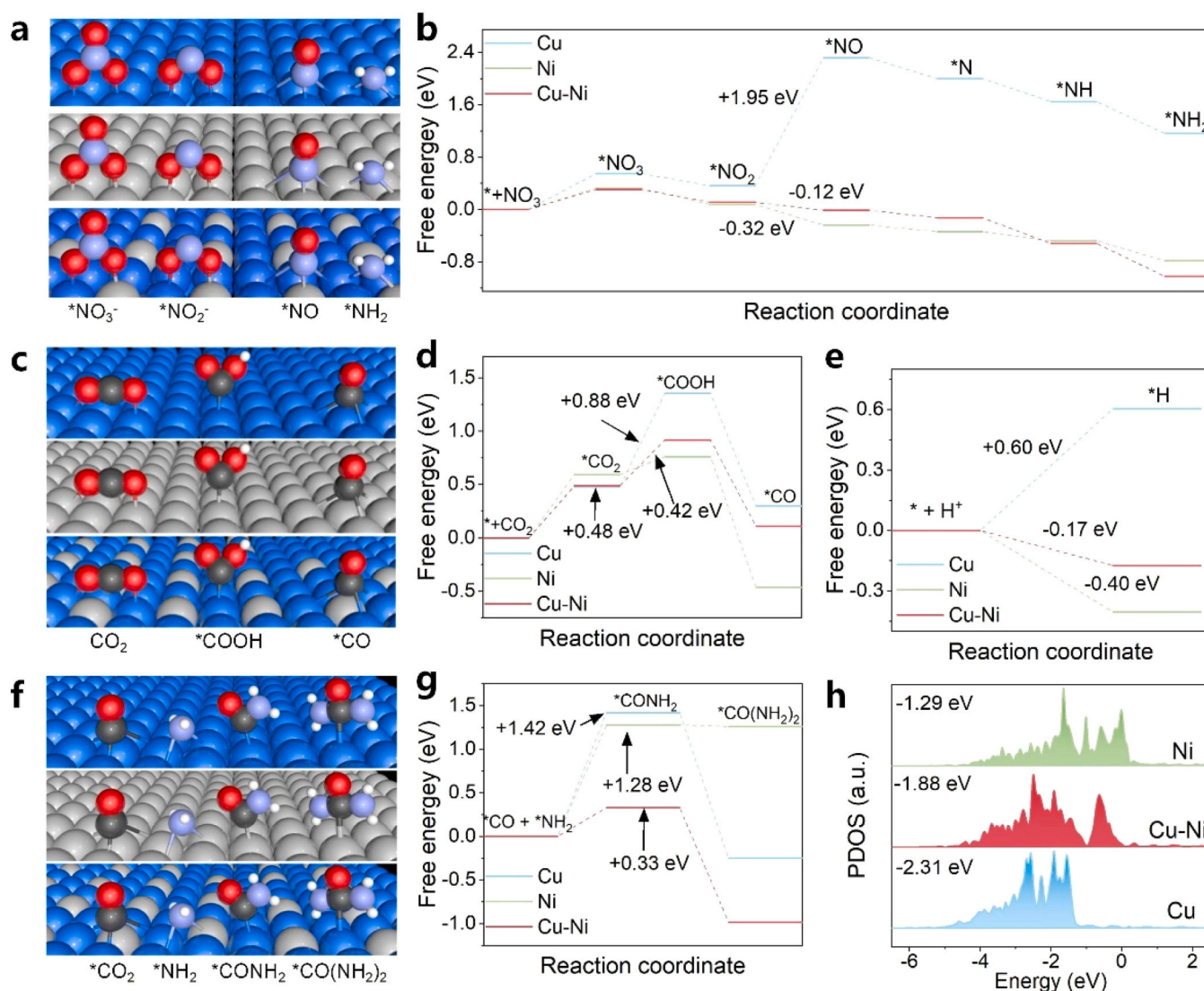


Fig. 5. DFT calculations. (a) Schematic model of the adsorption of intermediate and (b) free energy profile of NO_3^- reduction to $^*\text{NH}_2$. (c) Schematic model of the intermediate adsorption and (d) free energy profile of CO_2 reduction to $^*\text{CO}$. (e) Free energy profile of H^+ reduction to $^*\text{H}$. (f) Schematic model of the intermediate and (g) free energy profile of C–N coupling on Cu, Ni, and Cu–Ni alloy surfaces. (h) Electronic partial density of states in 3d orbitals and d-band center positions of Cu, Ni, and Cu–Ni alloy. “*” represents the adsorbed state.

is difficult to produce protons ($^*\text{H}$) on Cu atoms with Gibbs free energy change (ΔG) of 0.60 eV. The doping of Ni facilitates such a process and makes hydrogenation a spontaneous process, which greatly promotes the conversion of $^*\text{NO}_2$ to $^*\text{NH}_2$.

The schematic model of the intermediate for the reduction of CO_2 to $^*\text{CO}$ (Fig. 5c and Table S3) shows that the C atoms in $^*\text{CO}$ adsorbed by Cu, Ni and Cu-Ni alloy are preferred to bond with Cu atoms. The Gibbs free energy of the reaction are presented in Fig. 5d, and the Gibbs free energy of $^*\text{COOH}$ formation ($\Delta G = 0.88$ eV) becomes the potential limiting step on Cu. The doping of Ni may lead to the change of electronic states of Cu atoms (will be discussed later), resulting in enhanced adsorption of Cu to $^*\text{COOH}$ and $^*\text{CO}$ [49,50]. Fig. 5f presents the C–N couplings between $^*\text{CO}$ and $^*\text{NH}_2$. In comparison with the Cu or Ni metals, the $^*\text{CO}$ and $^*\text{NH}_2$ prefer to heterogeneously bond with both Cu and Ni atoms in DFT optimization process. In such an adsorption model, the $^*\text{CO}$ is adsorbed on Ni site and the $^*\text{NH}_2$ is adsorbed on Cu site. As illustrated in Fig. 5g, C–N coupling is an important rate-determining step. The ΔG of $^*\text{CO}$ and $^*\text{NH}_2$ for Ni and Cu is 1.42 and 1.28 eV, respectively. As for Cu-Ni alloy, as the $^*\text{CO}$ adsorbs on Cu site and $^*\text{NH}_2$ adsorbs on Cu and Ni site, the ΔG of $^*\text{CO}$ and $^*\text{NH}_2$ coupling decreased to only 0.33 eV, which greatly promotes the urea formation. The second step of C–N coupling between $^*\text{NH}_2\text{CO}$ and $^*\text{NH}_2$ is a thermodynamically spontaneous process for Cu and Cu-Ni and needs relatively large energy input for Ni. Therefore, Ni atoms act as the active site of $^*\text{NH}_2$ and Cu atoms act as the active site of $^*\text{CO}$ to synergistically achieve C–N coupling reactions. Furthermore, after incorporation of Ni, the d-band center of Cu-Ni alloy upshifts toward the Fermi level in comparison with the Cu, as the Fig. 5h exhibited. The changes of d-band center can also influence the adsorption and desorption ability of intermediate such as $^*\text{CO}$, $^*\text{CO}_2$, $^*\text{NO}_2$, and $^*\text{NH}_2$ [26,49].

4. Conclusion

In conclusion, the Ni is incorporated into Cu to form Cu-Ni alloys nanocrystals, acting as heterogeneous active sites for enhancing the hydrogenation of NO_x species and C–N coupling reactions to produce urea. Experimentally, the Cu supported Cu-Ni catalysts are synthesized by pyrolysis of Cu-Ni MOF. The analysis of EXAFS and XPS shows that Cu and Ni are mainly in metallic state alloy. The performance of urea synthesis for Cu-Ni catalyst is higher than those of elemental metal Cu and Ni, which achieves urea Faradaic efficiency to 25.1 % at -0.5 V (vs RHE) and yield of $37.53 \mu\text{mol h}^{-1} \text{cm}^{-2}$ at -0.8 V (vs RHE). The performance of Ni-Cu alloy is much superior to mostly reported catalysts. The pathway of urea formation is analyzed by in situ FTIR, suggesting a possible C–N coupling reaction pathway between $^*\text{NH}_2$ and $^*\text{CO}$. The theoretical calculations reveal that hydrogenation of $^*\text{NO}_x$ and coupling of $^*\text{CO}$ and $^*\text{NH}_2$ are more easily occurred over the heterogeneous Cu and Ni atoms rather than on homogeneous Cu and Ni atoms. The constructed heterogeneous active sites reported in this work give an efficient strategy to promote electrochemical urea synthesis from NO_3^- and CO_2 .

CRediT authorship contribution statement

Yulong Zhou: Data curation, Writing- Original draft preparation. **Baopeng Yang:** Conceptualization, Methodology. **Zhencong Huang:** Validation. **Gen Chen:** Supervision. **Jianguo Tang:** Visualization. **Min Liu:** Software. **Xiaohu Liu:** Methodology. **Renzhi Ma:** Methodology. **Zongwei Mei:** Writing- Reviewing. **Ning Zhang:** Supervision, Conceptualization, Writing- Reviewing and Editing.

Declaration of Competing Interest

The authors declare that they have no known competing financial interests or personal relationships that could have appeared to influence the work reported in this paper.

Data availability

Data will be made available on request.

Acknowledgments

We appreciated the financial supports from the following fundings: National Natural Science Foundation of China (22072183); The Natural Science Foundation of Hunan Province, China (2022JJ30690); Foundation of Yangtze Delta Region Institute (Huzhou) of UESTC, China (Nos. U03210060); High Performance Computing Center of Central South University.

Appendix A. Supporting information

Supplementary data associated with this article can be found in the online version at doi:10.1016/j.apcatb.2023.123577.

References

- [1] S.-K. Geng, Y. Zheng, S.-Q. Li, H. Su, X. Zhao, J. Hu, H.-B. Shu, M. Jaroniec, P. Chen, Q.-H. Liu, S.-Z. Qiao, Nickel ferrocyanide as a high-performance urea oxidation electrocatalyst, *Nat. Energy* 6 (2021) 904–912.
- [2] R. Lan, S.W. Tao, J.T.S. Irvine, A direct urea fuel cell - power from fertiliser and waste, *Energy Environ. Sci.* 3 (2010) 438–441.
- [3] V. Kyriakou, I. Garagounis, A. Vourros, E. Vasileiou, M. Stoukides, An electrochemical Haber-Bosch process, *Joule* 4 (2020) 142–158.
- [4] A.J. Martín, T. Shinagawa, J. Pérez-Ramírez, Electrocatalytic reduction of nitrogen: from Haber-Bosch to ammonia artificial leaf, *Chem* 5 (2019) 263–283.
- [5] X.Y. Liu, A. Elgowainy, M. Wang, Life cycle energy use and greenhouse gas emissions of ammonia production from renewable resources and industrial by-products, *Green. Chem.* 22 (2020) 5751–5761.
- [6] C.D. Lv, L.X. Zhong, H.J. Liu, Z.W. Fang, C.S. Yan, M.X. Chen, Y. Kong, C. Lee, D. B. Liu, S.Z. Li, J.W. Liu, S. Li, G. Chen, Q.Y. Yan, G.H. Yu, Selective electrocatalytic synthesis of urea with nitrate and carbon dioxide, *Nat. Sustain.* 4 (2021) 868–876.
- [7] B.H.R. Suryanto, H.L. Du, D.B. Wang, J. Chen, A.N. Simonov, D.R. MacFarlane, Challenges and prospects in the catalysis of electroreduction of nitrogen to ammonia, *Nat. Catal.* 2 (2019) 290–296.
- [8] C. Chen, N. He, S. Wang, Electrocatalytic C–N coupling for urea synthesis, *Small Sci.* 1 (2021) 2100070.
- [9] J. Li, G. Zhan, J. Yang, F. Quan, C. Mao, Y. Liu, B. Wang, F. Lei, L. Li, A.W.M. Chan, L. Xu, Y. Shi, Y. Du, W. Hao, P.K. Wong, J. Wang, S.X. Dou, L. Zhang, J.C. Yu, Efficient ammonia electrosynthesis from nitrate on strained ruthenium nanoclusters, *J. Am. Chem. Soc.* 142 (2020) 7036–7046.
- [10] Y.C. Zeng, C. Priest, G.F. Wang, G. Wu, Restoring the nitrogen cycle by electrochemical reduction of nitrate: progress and prospects, *Small Methods* 4 (2020) 28.
- [11] J.Y. Fang, Q.Z. Zheng, Y.Y. Lou, K.M. Zhao, S.N. Hu, G. Li, O. Akdim, X.Y. Huang, S.G. Sun, Ampere-level current density ammonia electrochemical synthesis using CuCo nanosheets simulating nitrite reductase bifunctional nature, *Nat. Commun.* 13 (2022) 7899.
- [12] N. Meng, X. Ma, C. Wang, Y. Wang, R. Yang, J. Shao, Y. Huang, Y. Xu, B. Zhang, Y. Yu, Oxide-derived core-shell Cu@Zn nanowires for urea electrosynthesis from carbon dioxide and nitrate in water, *ACS Nano* 16 (2022) 9095–9104.
- [13] Z. Mei, Y. Zhou, W. Lv, S. Tong, X. Yang, L. Chen, N. Zhang, Recent progress in electrocatalytic urea synthesis under ambient conditions, *ACS Sustain. Chem. Eng.* 10 (2022) 12477–12496.
- [14] X. Zhang, X. Zhu, S. Bo, C. Chen, M. Qiu, X. Wei, N. He, C. Xie, W. Chen, J. Zheng, P. Chen, S.P. Jiang, Y. Li, Q. Liu, S. Wang, Identifying and tailoring C–N coupling site for efficient urea synthesis over diatomic Fe-Ni catalyst, *Nat. Commun.* 13 (2022) 5337.
- [15] X. Wei, X. Wen, Y. Liu, C. Chen, C. Xie, D. Wang, M. Qiu, N. He, P. Zhou, W. Chen, J. Cheng, H. Lin, J. Jia, X.Z. Fu, S. Wang, Oxygen vacancy-mediated selective C–N coupling toward electrocatalytic urea synthesis, *J. Am. Chem. Soc.* 144 (2022) 11530–11535.
- [16] Y. Liu, X. Tu, X. Wei, D. Wang, X. Zhang, W. Chen, C. Chen, S. Wang, C-Bound or O-Bound Surface: which one boosts electrocatalytic urea synthesis? *Angew. Chem. Int. Ed. Engl.* 62 (2023), e202300387.
- [17] M. Shibata, K. Yoshida, N. Furuya, Electrochemical synthesis of urea on reduction of carbon dioxide with nitrate and nitrite ions using Cu-loaded gas-diffusion electrode, *J. Electroanal. Chem.* 387 (1995) 143–145.
- [18] M. Shibata, K. Yoshida, N. Furuya, Electrochemical synthesis of urea at gas-diffusion electrodes: IV. Simultaneous Reduction of carbon dioxide and nitrate ions with various metal catalysts, *J. Electrochem. Soc.* 145 (1998) 2348.
- [19] J. Jang, S. Zhu, E.P. Delmo, T. Li, Q. Zhao, Y. Wang, L. Zhang, H. Huang, J. Ge, M. Shao, Facile design of oxide-derived Cu nanosheet electrocatalyst for CO_2 reduction reaction, *EcoMat* 5 (2023), e12334.
- [20] R. Ding, G. Fu, S. Wang, Y. Yang, Q. Lang, H. Zhao, X. Yang, V. Valtchev, The activity of ultrafine Cu clusters encapsulated in nano-zeolite for selective hydrogenation of CO_2 to methanol, *Catalysts* (2022).

- [21] C. Li, S. Liu, Y. Xu, T. Ren, Y. Guo, Z. Wang, X. Li, L. Wang, H. Wang, Controllable reconstruction of copper nanowires into nanotubes for efficient electrocatalytic nitrate conversion into ammonia, *Nanoscale* 14 (2022) 12332–12338.
- [22] J. Leverett, T. Tran-Phu, J.A. Yuwono, P. Kumar, C. Kim, Q. Zhai, C. Han, J. Qu, J. Cairney, A.N. Simonov, R.K. Hocking, L. Dai, R. Daiyan, R. Amal, Tuning the coordination structure of Cu-N-C single atom catalysts for simultaneous electrochemical reduction of CO₂ and NO₃⁻ to urea, *Adv. Energy Mater.* 12 (2022) 2201500.
- [23] S. Nitopi, E. Bertheussen, S.B. Scott, X. Liu, A.K. Engstfeld, S. Horch, B. Seger, I.E. L. Stephens, K. Chan, C. Hahn, J.K. Nørskov, T.F. Jaramillo, I. Chorkendorff, Progress and perspectives of electrochemical CO(2) reduction on copper in aqueous electrolyte, *Chem. Rev.* 119 (2019) 7610–7672.
- [24] J. Geng, S. Ji, M. Jin, C. Zhang, M. Xu, G. Wang, C. Liang, H. Zhang, Ambient electrosynthesis of urea with nitrate and carbon dioxide over iron-based dual-sites, *Angew. Chem. Int. Ed. Engl.* 62 (2023), e202210958.
- [25] S. Payra, N. Devaraj, K. Tarafder, S. Roy, Unprecedented electroreduction of CO₂ over Metal organic framework-derived intermetallic nano-alloy Cu_{0.85}Ni_{0.15}/C, *ACS Appl. Energy Mater.* 5 (2022) 4945–4955.
- [26] Y. Wang, A. Xu, Z. Wang, L. Huang, J. Li, F. Li, J. Wicks, M. Luo, D.H. Nam, C. S. Tan, Y. Ding, J. Wu, Y. Lum, C.T. Dinh, D. Sinton, G. Zheng, E.H. Sargent, Enhanced nitrate-to-ammonia activity on copper-nickel alloys via tuning of intermediate adsorption, *J. Am. Chem. Soc.* 142 (2020) 5702–5708.
- [27] Y. Deng, A.D. Handoko, Y. Du, S. Xi, B.S. Yeo, In situ Raman spectroscopy of copper and copper oxide surfaces during electrochemical oxygen evolution reaction: identification of cu(II) oxides as catalytically active species, *ACS Catal.* 6 (2016) 2473–2481.
- [28] D.T. Zhang, K. Yamamoto, Y.C. Wang, S.H. Gao, T. Uchiyama, T. Watanabe, T. Takami, T. Matsunaga, K. Nakanishi, H. Miki, H. Iba, K. Amezawa, K. Maeda, H. Kageyama, Y. Uchimoto, Reversible and fast (De)fluorination of high-capacity Cu₂O cathode: one step toward practically applicable all-solid-state fluoride-ion battery, *Adv. Energy Mater.* 11 (2021) 2102285.
- [29] D. Wang, Q. Li, C. Han, Q. Lu, Z. Xing, X. Yang, Atomic and electronic modulation of self-supported nickel-vanadium layered double hydroxide to accelerate water splitting kinetics, *Nat. Commun.* 10 (2019) 3899.
- [30] D. Wang, C. Han, Z. Xing, Q. Li, X. Yang, Pt-like catalytic behavior of MoNi decorated CoMoO₃ cuboid arrays for the hydrogen evolution reaction, *J. Mater. Chem. A* 6 (2018) 15558–15563.
- [31] S. Neatu, J.A. Macia-Agullo, P. Concepcion, H. Garcia, Gold-copper nanoalloys supported on TiO₂ as photocatalysts for CO₂ reduction by water, *J. Am. Chem. Soc.* 136 (2014) 15969–15976.
- [32] Y. Bu, C. Wang, W. Zhang, X. Yang, J. Ding, G. Gao, Electrical pulse-driven periodic self-repair of Cu-Ni tandem catalyst for efficient ammonia synthesis from nitrate, *Angew. Chem. Int. Ed. Engl.* 62 (2023), e202217337.
- [33] M. Yuan, J. Chen, Y. Bai, Z. Liu, J. Zhang, T. Zhao, Q. Wang, S. Li, H. He, G. Zhang, Unveiling electrochemical urea synthesis by co-activation of CO(2) and N(2) with Mott-Schottky heterostructure catalysts, *Angew. Chem. Int. Ed. Engl.* 60 (2021) 10910–10918.
- [34] L. Li, C. Tang, X. Cui, Y. Zheng, X. Wang, H. Xu, S. Zhang, T. Shao, K. Davey, S. Z. Qiao, Efficient nitrogen fixation to ammonia through integration of plasma oxidation with electrocatalytic reduction, *Angew. Chem. Int. Ed. Engl.* 60 (2021) 14131–14137.
- [35] Y. Zhao, R. Shi, X. Bian, C. Zhou, Y. Zhao, S. Zhang, F. Wu, G.I.N. Waterhouse, L. Z. Wu, C.H. Tung, T. Zhang, Ammonia detection methods in photocatalytic and electrocatalytic experiments: how to improve the reliability of NH(3) production rates? *Adv. Sci. (Weinh.)* 6 (2019) 1802109.
- [36] D. Li, N. Xu, Y. Zhao, C. Zhou, L.P. Zhang, L.Z. Wu, T. Zhang, A reliable and precise protocol for urea quantification in photo/electrocatalysis, *Small Methods* 6 (2022), e2200561.
- [37] J. Cai, J. Huang, A. Cao, Y. Wei, H. Wang, X. Li, Z. Jiang, G.I.N. Waterhouse, S. Lu, S.-Q. Zang, Interfacial hydrogen bonding-involved electrocatalytic ammonia synthesis on OH-terminated MXene, *Appl. Catal. B: Environ.* 328 (2023), 122473.
- [38] H. Song, M. Wu, Z. Tang, J.S. Tse, B. Yang, S. Lu, Single atom ruthenium-doped CoP/CDs nanosheets via splicing of carbon-dots for robust hydrogen production, *Angew. Chem. -Int. Ed.* 60 (2021) 7234–7244.
- [39] E. Pérez-Gallent, M.C. Figueiredo, I. Katsounaros, M.T.M. Koper, Electrocatalytic reduction of Nitrate on Copper single crystals in acidic and alkaline solutions, *Electrochim. Acta* 227 (2017) 77–84.
- [40] Q. Hu, Y. Qin, X. Wang, Z. Wang, X. Huang, H. Zheng, K. Gao, H. Yang, P. Zhang, M. Shao, C. He, Reaction intermediate-mediated electrocatalyst synthesis favors specified facet and defect exposure for efficient nitrate–ammonia conversion, *Energy Environ. Sci.* 14 (2021) 4989–4997.
- [41] D. Yue, Y. Jia, Y. Yao, J. Sun, Y. Jing, Structure and electrochemical behavior of ionic liquid analogue based on choline chloride and urea, *Electrochim. Acta* 65 (2012) 30–36.
- [42] M. Szafran, Z. Dega-Szafran, A. Addlagatta, M. Jaskolski, Crystal structure and vibrational spectrum of N-methylpiperidine betaine hexafluorosilicate, *J. Mol. Struct.* 598 (2001) 267–276.
- [43] H. Lin, S.R. Bean, M. Tilley, K.H.S. Peiris, D. Brabec, Qualitative and quantitative analysis of sorghum grain composition including protein and tannins Using ATR-FTIR spectroscopy, *Food Anal. Methods* 14 (2021) 268–279.
- [44] K. Karmali, A. Karmali, A. Teixeira, M.J. Curto, The use of Fourier transform infrared spectroscopy to assay for urease from *Pseudomonas aeruginosa* and *Canavalia ensiformis*, *Anal. Biochem.* 331 (2004) 115–121.
- [45] M. Sun, G. Wu, J. Jiang, Y. Yang, A. Du, L. Dai, X. Mao, Q. Qin, Carbon-anchored molybdenum oxide nanoclusters as efficient catalysts for the electrosynthesis of ammonia and urea, *Angew. Chem. Int. Ed. Engl.* 62 (2023), e202301957.
- [46] R. Sipieha, FTIR-ATR spectra of protein A immobilized on to functionalized polypropylene membranes by gaseous plasma of oxygen and of anhydrous ammonia, *Biomater. Artif. Cells Artif. Organs* 16 (1988) 955–966.
- [47] M.F. Kadir, Z. Aspanut, S.R. Majid, A.K. Arof, FTIR studies of plasticized poly(vinyl alcohol)-chitosan blend doped with NH₄NO₃ polymer electrolyte membrane, *Spectrochim. Acta A Mol. Biomol. Spectrosc.* 78 (2011) 1068–1074.
- [48] T. Hu, C. Wang, M. Wang, C.M. Li, C. Guo, Theoretical insights into superior nitrate reduction to ammonia performance of copper catalysts, *ACS Catal.* 11 (2021) 14417–14427.
- [49] M. Ma, H.A. Hansen, M. Valenti, Z. Wang, A. Cao, M. Dong, W.A. Smith, Electrochemical reduction of CO₂ on compositionally variant Au-Pt bimetallic thin films, *Nano Energy* 42 (2017) 51–57.
- [50] H. Cheng, Z. Fan, X. Wu, M. Feng, W. Zheng, G. Lei, X. Li, F. Cui, G. He, Coordination engineering of the hybrid Co-C and Co-N active sites for efficient catalyzing CO₂ electroreduction, *J. Catal.* 405 (2022) 634–640.